Maddalena, Riccardo 2019. Effect of silica particle size on the formation of calcium silicate hydrate using thermal analysis. Thermochimica Acta 672 , pp. 142-149. 10.1016/j.tca.2018.09.003

Publishers page: https://doi.org/10.1016/j.tca.2018.09.003

Title: Effect of silica particle size on the formation of calcium silicate hydrate using thermal analysis

Author: Riccardo Maddalena Christopher Hall Andrea Hamilton

PII: S0040-6031(18)30732-9
DOI: https://doi.org/doi:10.1016/j.tca.2018.09.003
Reference: TCA 78087

To appear in: *Thermochimica Acta*

Received date: 18-9-2017
Revised date: 4-8-2018
Accepted date: 2-9-2018

Please cite this article as: Riccardo Maddalena, Christopher Hall, Andrea Hamilton, Effect of silica particle size on the formation of calcium silicate hydrate using thermal analysis, *<![CDATA[Thermochimica Acta]]>* (2018), https://doi.org/10.1016/j.tca.2018.09.003

- C-S-H pastes made with two different silica particle sizes are investigated.
- Isothermal calorimetry is used to study the effect of particle size on the stoichiometry.
- The overall kinetics are well described by a simple exponential (first-order) reaction model

Effect of silica particle size on the formation of calcium silicate hydrate using thermal analysis

Riccardo Maddalena[a,c], Christopher Hall[b], Andrea Hamilton*[a]

[a] *University of Strathclyde, Department of Civil and Environmental Engineering, Glasgow G1 1XJ, UK*
[b] *University of Edinburgh, School of Engineering, Edinburgh EH9 3JL, UK*
[c] *Cardiff University, School of Engineering, Cardiff CF24 3AA, UK*

Abstract

Calcium silicate hydrate (C-S-H) is made by mixing calcium hydroxide (portlandite), silica and water at two calcium oxide to silica (C/S) ratios, using nanosilica and silica fume. We investigate how silica particle size influences the rate and extent of formation of C-S-H at room temperature by isothermal calorimetry, thermal analysis, Raman spectroscopy and X-ray diffraction. Rate of reaction increases as silica particle size decreases, and is five times greater with nanosilica than with silica fume. Final composition depends only on initial C/S ratio. Compositions at 28 days are estimated from thermogravimetric and X-ray diffraction data. There is a weak maximum in the reaction rate of nanosilica pastes about 20–30h after mixing. The overall kinetics are well described by a simple exponential (first-order) reaction model. The early-time reaction rate around the rate maximum is described by an Avrami model.

Keywords: calcium silicate hydrate, nano-silica, silica fume, heat of hydration, calorimetry, Raman spectra

---

1. Introduction

Increasing awareness of climate change and greenhouse gas emissions has led researchers to develop alternative materials to control the environmental impact of manufacturing industries. Cement production is responsible for about 7–10% of the total anthropogenic CO_2 emissions [1]. In recent years cement has been partially replaced by the addition of waste by-products such as fly ash and amorphous silica [2, 3, 4, 1, 5]. Fly ash is well established in the cement industry as an environmentally friendly replacement for cement at up to 35 wt% [6], without compromising the mechanical and physical properties of concrete [7]. Amorphous forms of silica, such as silica fume and nano-silica, have also been investigated. Silica fume is a by-product of the silicon and ferro-silicon industry, with a nominal particle size range of 100–1000 nm, while commercial nano-silica is *ad-hoc* synthesised from sodium silicate using a sol-gel technique. Recent investigations have also explored the production of 'green' nano-silica from waste dunite, which has a comparatively lower environmental footprint [8]. Silica fume has been shown to enhance the mechanical strength of Portland cement, reduce permeability and thermal conductivity [9, 10, 1], and accelerate the early hydration of C_2S, C_3A and C_4AF [11], while nano-silica enhances strength from increased production of additional C-S-H [4]. (Here we use the standard abbreviations $C = CaO$, $S = SiO_2$, $H = H_2O$ generally employed in cement chemistry). The smaller particle size of nano-silica produces a correspondingly greater surface area to provide nucleation sites for the growth of C-S-H [12, 13].

Thermal analytical techniques are extremely useful not only in understanding the hydration kinetics of cement, but also in providing reaction models to tailor cement paste for specific applications. Kumar *et al.* [14] studied the effect of fly ash on the hydration of ordinary Portland cement by isothermal calorimetry and found that while the addition of 20 wt% fly ash retards the hydration, this effect is negated by addition of 5 wt% of calcium hydroxide. Wei *et al.* [11] used TG/DSC to study hydrated cement modified by silica fume. They found that silica fume accelerates the early hydration of cement and stabilizes ettringite, and therefore reduces damage to the set cement and concrete from delayed ettringite formation. However, when silica-fume is combined with fly ash, the overall effect is a delayed hydration [15]. Oltulu and Sahin (2014) [16] studied the pore-structure development of cement mortars containing silica fume and other nano-powders. The addition of nano-silica resulted in an increased amount of C-S-H and other hydrated products. On the other hand, it has been shown that an increasing content of silica fume in Portland cement results in a lower C/S ratio of the C-S-H [17]. Thermogravimetric analysis and calorimetry data have been used to determine the pozzolanic reaction of supplementary cementitious materials (such as fly ash) and to describe the cement or concrete hydration reaction, and validated results were useful in establishing models for the hydration of cement [18, 19]. Although there are several experimental reports of the beneficial effects of amorphous silica added to cement, little research has been conducted on the effect of silica particle size on the formation of the C-S-H phases responsible for early strength and hardening [20]. This is partly due to the difficulty of accurately quantifying the C-S-H content when it is found among other hydrated products such as ettringite and the calcium aluminate hydrates [20]. Nonetheless, the C-S-H formed in cement by hydration of alite (C_3S) and belite (C_2S) or in cement-alkali systems is morphologically different from synthetic C-S-H. In the first case C-S-H assumes the typical fibrillar habit, whereas in synthetic formation it tends to form with a two-dimensional 'crumpled foil' habit which, according to Richardson [21, 22], indicates that the C-S-H has less space constraint during growth. A clearer understanding of C-S-H behaviour is obtained by isolating it from other accessory minerals, while the behaviour of pure C-S-H (made without the hydration of Portland cement clinker) is of significant relevance to the fields of nuclear waste and environmental contaminant trapping as C-S-H is the component which adsorbs.

In this work we prepared C-S-H in isolation from other mineral phases, and studied its formation by thermal analysis and isothermal calorimetry, supported by Raman spectroscopy and X-ray diffraction. We synthesised C-S-H by reacting calcium hydroxide with silica and varying the calcium to silica (C/S) ratios. The effect of the silica particle size on the formation of C-S-H was investigated using two different silica sources: silica fume (particle size range 100–1000 nm) and nano-silica (particle size range 5–20 nm). We show how silica particle size and hydration kinetics affect the extent of reaction at 28 days and the final composition.

2. Materials and methods

2.1. Materials

C-S-H phases were synthesised using reagent grade calcium hydroxide (portlandite) powder (Sigma Aldrich, CAS number 1305-62-0), aqueous-suspension nano-silica (Sigma Aldrich Ludox T50 nano-SiO_2, CAS number 7631-86-9), and silica fume SF920D (Elkem Microsilica, Norway, CAS number 69012-64-2). To minimise carbonation during mixing, deionised and decarbonated water was used [23]. Physicochemical properties of the starting materials are reported in Table 1. X-ray patterns (Figure 1) show that the silica fume and nano-silica particles used are essentially amorphous.

Table 1: Properties of calcium hydroxide (CH), nano-silica suspension Ludox T50 (NS), and silica fume SF920D (SF)

Material	Calcium hydroxide	Nano-silica (NS)	Silica fume (SF)
Form	Dry powder	Suspension in H_2O	Dry powder
Assay	$Ca(OH)_2$: $\geq$ 95.0%	SiO_2: 50.0%	SiO_2: $\geq$ 90.0%
	Reagent grade		
	$CaCO_3$: $\leq$ 3.0		
Anion traces	Cl^-: $\leq$ 0.03%	Cl^-: $\leq$ 0.05%	
Cation traces	Na, K, Mg $\leq$ 0.05%		
pH at 25 °C	12.4 (slurry)	8.5–9.5	–
Particle size range (nm)	–	5-20	100–1000
Density at 25 °C (g cm^{-3})	2.24	1.40	2.2–2.3
Specific area (m^2 g^{-1})	20–41 (hydrated)	110–150	15–30

C-S-H pastes were mixed manually in a nitrogen environment at room temperature. Calcium hydroxide, silica (either silica fume or nano-silica) and water were mixed at a liquid:solid weight ratio of 2.0. Two different target lime (CaO) to silica (C/S) ratios, 0.81 and 2.4 mol/mol, were investigated (Table 2). These

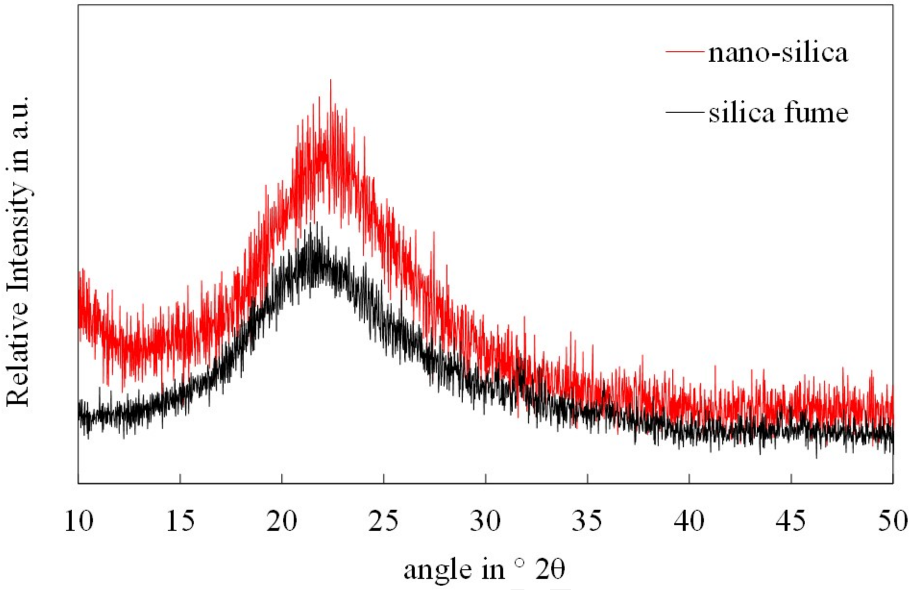

Figure 1: X-ray diffraction patterns of amorphous silica fume and nano-silica, showing broad diffuse scattering.

mol ratios correspond to the ratios 1:1 and 3:1 portlandite:silica by weight. Specimens were cast in cube moulds, stored in a sealed environment at 20 °C, 100% RH, and cured for 28 days. After curing, the samples were demoulded, immersed in an acetone bath for 24 h to arrest the hydration process [24, 25], and then placed in a drying chamber under a nitrogen flow. All samples were then ground by hand and sieved to obtain a homogeneous fine powder, and stored in a sealed environment.

2.2. Materials characterisation and thermal analysis

Powder XRD analyses were performed using a Bruker D8 Advance diffractometer with CuKα radiation over the range 10–60° 2θ, step size of 0.02° and scan rate of 0.5 s/step. The samples were also characterised by Raman spectroscopy, using a Renishaw InVia spectrometer equipped with Modulaser Stellar Pro ML/150 argon ion laser (785 nm). Raman shifts were recorded over a

Table 2: Sample mixes, silica source (silica fume, SF or nano-silica, NS), and initial mix and paste compositions

Mix ID	Silica source	Initial mix composition CH/S by wt	C/S mol/mol	CH g/g paste	S
SF24	SF	3:1	2.4	0.25	0.083
SF081	SF	1:1	0.81	0.167	0.167
NS24	NS	3:1	2.4	0.25	0.083
NS081	NS	1:1	0.81	0.167	0.167

9 point map (200 × 200 μm) and wave-number range of 100–4000 cm^{-1}, using the ×20 objective lens. The exposure time was 10 s, and each spectrum was accumulated three times. Peaks were fitted to a gaussian lineshape using PeakFit (T.C. O'Haver) in Matlab. Specific heat flow and heat of reaction were measured using an isothermal calorimeter (I-Cal 4000 HPC, Calmetrix). Fresh paste (about 40 g) was cast into a cylindrical container and placed into the calibrated calorimeter, at a constant temperature of 21 ± 2 °C. The heat flow was recorded over 200 h. Samples were mixed externally, hence the first 5–10 min of detected heat flow were not taken into account for further calculations. Thermo-gravimetric (TG) and differential scanning calorimetry (DSC) data were collected using a NETSZCH STA 449 F1 Jupiter instrument. Measurements were made on 10–20 mg powder samples, under constant nitrogen flow at a heating rate of 10 °C min^{-1} from 25 °C to 1000 °C. Results are plotted as weight loss (%) and heat flow ($\mathrm{mW\,mg}^{-1}$) as a function of the temperature (°C). TG measurement results were also used to calculate the final C/S molar ratio of the samples, according to the methodology of Garbev *et al.* [26].

3. Results and discussions

3.1. XRD characterisation and Raman spectroscopy

XRD patterns were obtained on specimens of all four mixes at 28 d (Fig 2). These were intended primarily to provide information on mineralogy and structure, but quantitative peak-area analysis also provides support for the TGA composition results. The XRD patterns show the main features expected of

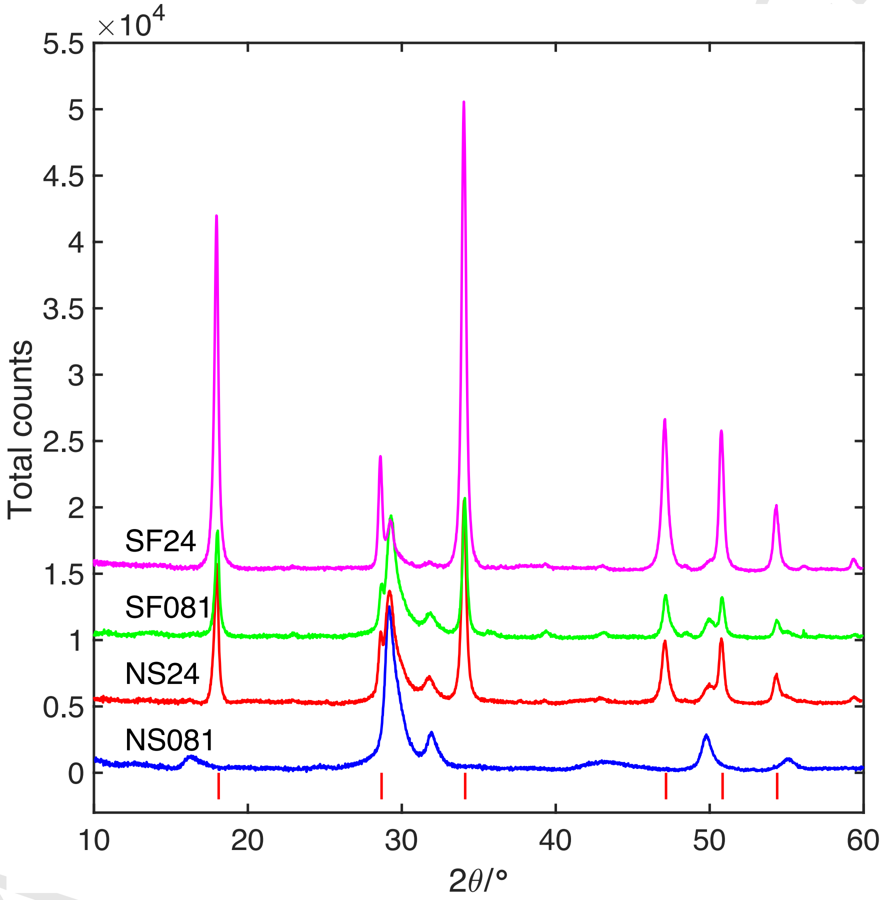

Figure 2: XRD patterns of dried solid material from all mixes after 28 d reaction. Small zero corrections have been applied to the 2θ scale to align peak positions. The principal diffraction lines of portlandite are shown as red ticks.

C-S-H(I) [26, 27, 28, 29], namely a strong reflection at $\sim$29.3° 2θ, and other prominent reflections at $\sim$34.1°, $\sim$49.7°. These correspond to the (020), (200) and (240) reflections of tobermorite [27]. The (002) basal reflection at $\sim$6.6° was outside the scan range and was not observed.

In NS24, SF081 and SF24, portlandite was present, with principal peaks at the positions shown in Fig 2. In NS081, all of the portlandite in the original mix has been consumed, and we have an uncontaminated C-S-H pattern of low C/S ratio. We note that in all patterns the strong (020) peak at 29.3° is markedly asymmetric. The weak (101) reflection at $\sim$16.1° 2θ is visible only in the low C/S mixes NS081 and SF081, an observation consistent with the comment of Tajuelo Rodriguez *et al.* [28] who find that this peak decreases in intensity as the C/S ratio increases. Likewise the broad reflection at $\sim$44° is visible only in the NS081 pattern. A comparison of pseudo-Voigt peak areas allows us to estimate approximate compositions from the XRD patterns, using the NS081 pattern which contains no portlandite as a C-S-H reference. The estimated compositions from XRD are in good agreement with those from TGA (Table 6).

The Raman spectra of the samples are reported in Figure 3 with peak positions given in Table 3. The first low frequency bands in the range 200–305 cm^{-1} correspond to the Ca-O lattice vibrations in calcium carbonate. As demonstrated by Black *et al.* [30], these bands are only visible in samples which have begun to carbonate through exposure to air and are not present in fresh paste sealed from the environment. One is weakly present in NS081 at 279 cm^{-1} but it is poorly resolved compared to the bands at 270 and 302 cm^{-1} shown by Black *et al.* and our assignment is tentative. Carbonation is more obviously demonstrated in NS24, the sample with the highest C/S ratio and which contains 41 wt.% portlandite by the doublet at 1075 and 1085 cm^{-1}. Black *et al.* attribute this to the $\nu_1[CO_3]$ mode but it is significantly weaker than the very strong bands they find in samples exposed for 1 month. We conclude that our samples are lightly carbonated which fits with our sample preparation procedure. The presence of portlandite is clear from the intense peaks at c. 355

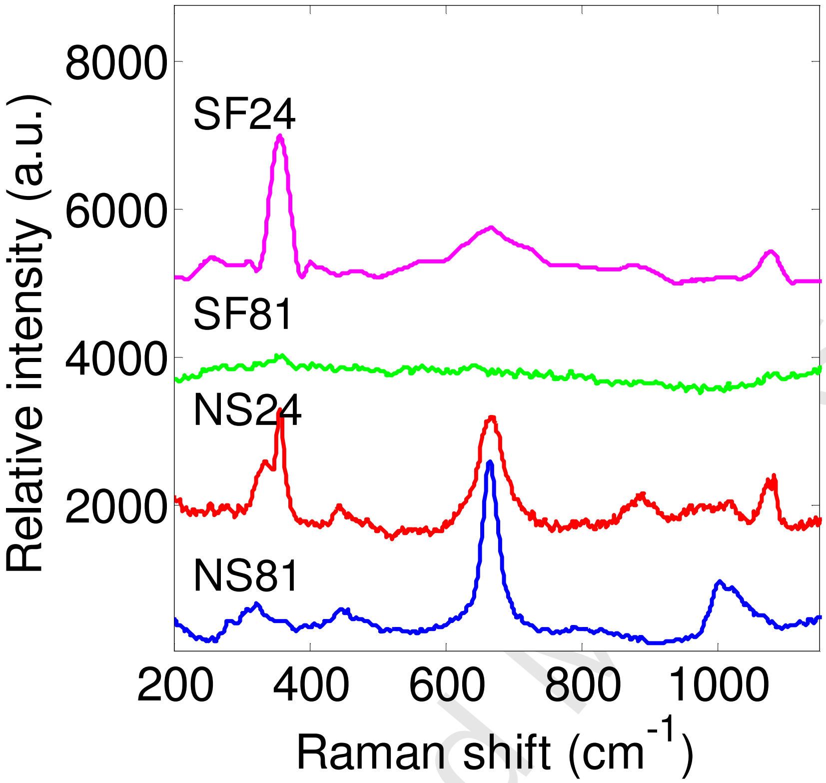

Figure 3: Raman spectra

cm^{-1} in the spectra for samples NS24 and SF24, which are assigned to Ca(OH)$_2$ external translation mode, A$_{1g}$ showing that the samples have not significantly carbonated as these bands are barely present after 40 hours of exposure in the carbonation study by Black *et al.* Ca-O lattice vibrations from C-S-H gel are described as occurring at 319 333 cm^{-1} in fresh samples of C/S ratio 0.5–1.5 [31] which broaden and move to lower frequencies upon carbonation, possibly due to weakening of the Ca-O bonds during C-S-H decalcification [30]. We see the band increase in frequency from 316–332 cm^{-1} as the C/S ratio increases from 0.79 (NS081) to 1.70 (NS24) which is in line with Garbev *et al.* The band at 445 cm^{-1}, attributed to O-Si-O bending vibrations in SiO$_4$ where the oxygen

Table 3: Position of the Raman peaks (cm^{-1}) for samples NS081, NS24 and SF24

NS081	NS24	SF24	Assignment
279 (w)	–	252	lattice vibrations, Ca-O in $CaCO_3$
316, 360 (w)	332	–	lattice vibrations, Ca-O in C-S-H
–	356 (vs)	354 (vs)	A_{1g} external translation mode in Ca(OH)2
446 (w)	447 (w)	–	SiO_4 mainly O(non)–Si–O(non) bending
665 (vs)	666 (s)	663	symmetric bending Si–O–Si, C-S-H
∼770–900	885	885	SiO_4 symmetric stretch of Q^1
∼1004	1018	1013	SiO_4 symmetric stretch of Q^2
–	1075, 1085	1079	CO_3 symmetric stretch

w: weak, s: strong, vs: very strong.

is non-bridging is present at 446 and 447 cm^{-1} in this work and is relatively weak, as shown in Figure 3. The strongest peak present in our spectra at 666 cm^{-1} is produced by Si-O-Si symmetric bending vibrations in C-S-H which have been shown to broaden with increasing C/S ratio from the presence of silicate dimers [31]. This effect can be seen in Figure 3 as the peak width increases (FWHM) from 28 (NS081, C/S=0.79) to 35 (NS24, C/S=1.70). A very weak peak at ∼885 cm^{-1} is visible in the higher C/S ratio samples (NS24 and SF24), which is assigned to the symmetric stretch of SiO_4) dimers (Q^1) by Garbev *et al.* who show it increases in intensity with increasing C/S ratio and is barely visible when the C/S ratio is less than 0.83. The peak at ∼1004 cm^{-1} in Figure 3 is strongest but also broadest in the spectra for NS081. The position is determined manually as the peak has a long asymmetric tail after the apex. This band is assigned to the symmetric stretch of SiO_4) chains (Q^2) and is described by Garbev *et al.* [31] as increasing in frequency with C/S ratio to a final value of 1022 cm^{-1} in samples with C/S 1.33 and 1.55. We see an increase in frequency from c. 1004 cm^{-1} at C/S = 0.79 to 1018 cm^{-1} at C/S = 1.70. The significant asymmetry of the peak in NS081 can be attributed to disorder in the silicate polymerisation and presence of different silicate species, such as long chains, octamers and pentamers [31]. The weak and comparatively narrow bands in NS24 and SF24 suggests only a few, uniform, Q^2 species are present [31]. As already discussed, CO_3 symmetric stretch ($\nu1$) modes occur at ~1080 cm^{-1} and are more clearly present in the samples with significant portlandite (SF24 and NS24) but are still weak by comparison with spectra from the 1 month old samples described by Black [30]. By comparison with NS spectra, the SF spectra, in particular SF81 are surprisingly featureless. Overall, the Raman spectra confirms the XRD and TGA evidence that there is only slight carbonation in the samples.

3.2. *Isothermal calorimetry*

The calorimetric heat flow rate (Figure 4) shows the following features:

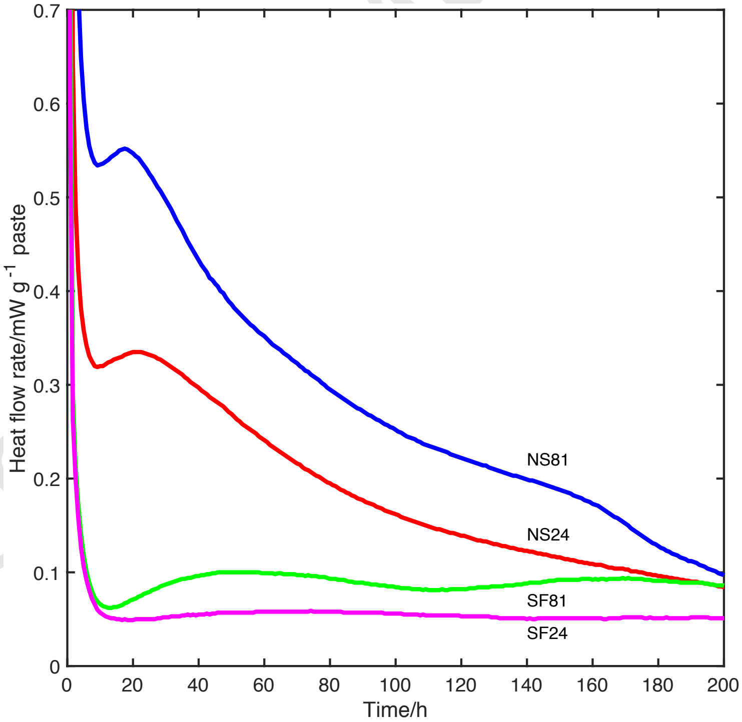

Figure 4: Heat flow rate for all mixes measured by isothermal calorimetry over a reaction time of 0–200 h.

1. An initial period of a few minutes in which the heat flow rate is high but falls rapidly; the heat evolved over this short initial period no doubt includes contributions from wetting and dissolution as well as early-time reaction, and also non-isothermal effects in the calorimeter.
2. A period of some hours in which the heat flow rate slowly decreases until a minimum is reached (the slow-rate or decelerating rate period).
3. After the minimum, the heat flow rate increases (the accelerating rate period) for some hours until it reaches a maximum.
4. Beyond the maximum, the heat-flow rate decreases slowly but in all cases is still measurable at 200 h.

We follow the usual practice of treating the calorimetric heat-flow rate after the initial period as a direct measure of the rate of formation of C-S-H. The features we identify are similar in several ways to those observed in calorimetric data for the hydration of tricalcium silicate C_3S [32, 20, 33, 34]. As here, C_3S hydration also shows a so-called slow-reaction period, followed by an accelerating period, which in turn is followed by a final extended period of decreasing heat flow rate. On the other hand, although the early-time minimum and maximum in the reaction rate are well defined, at least in the nano-silica systems, they are much less prominent than in C_3S hydration where the minimum heat-flow rate is close to zero [33]. Apart from these small variations in the hydration rate at early times, we find the overall hydration kinetics are accurately described by a simple exponential model. This is readily seen by considering the cumulative heat evolved (the area under the heat flow rate curve), which we can fit to the equation

$$H = b + H_0[1 - \exp(-kt)] \qquad (1)$$

where $H(t)$ is the cumulative heat evolved at time t, H_0 is the heat of reaction, k is a rate constant, and b is a constant to take account of initial heat-flow spike. Equation 1 is the standard first-order model of solid-state reaction kinetics [35]. Figure 5 shows that using data from about 50 h onwards allows us to extract values of rate constant k and heat of reaction H_0 for the four mixes. The

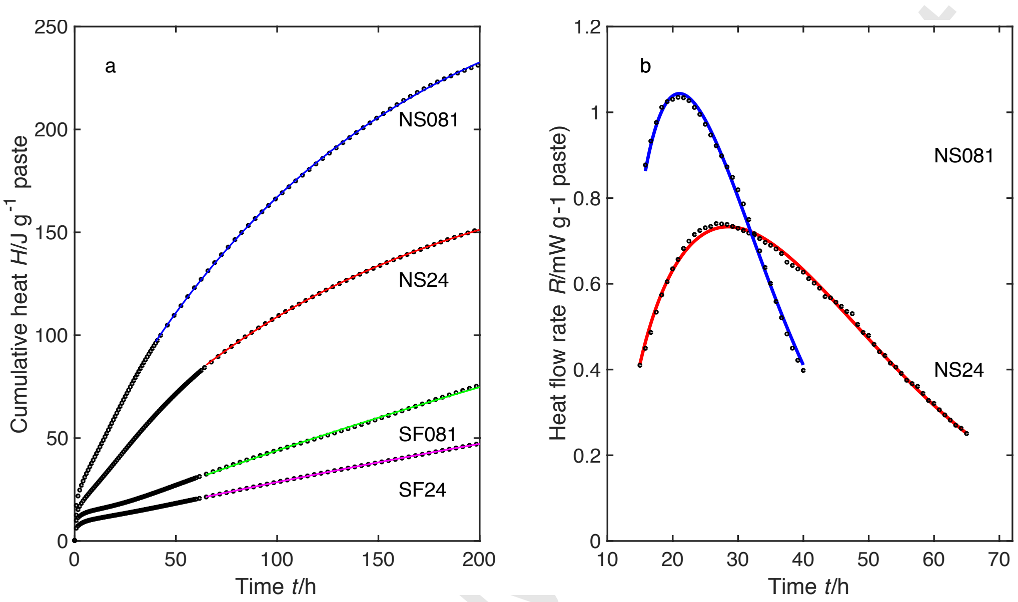

Figure 5: (a) Cumulative heat release H in the first 200 h of reaction, showing least-squares fits to Equation 1. (b) Heat flow rate R for nano-silica mixes NS81 and NS24, showing least-squares fits to Equation 3.

parameter values are given in Table 4.

The effect of particle size is clear from our (admittedly limited) data. The rate of hydration is much faster in the NS mixes than in the SF mixes, with k values being about five times smaller. This is approximately the same as the ratio of the specific surface areas (see Table 1), which is ∼5.8. The duration of the reaction can be estimated as $\tau = 4.61/k$, at which time the reaction is 99% complete. This shows that the NS mixes have fully reacted at 28 days. The SF mixes have only reached ∼60% of their final composition at 28 days, and take 4–5 months to reach 99 % completion. The parameter H_0 is also informative. The NS81 and SF81 mixes have the same silica content per unit weight of paste (Table 4), and we see that the ultimate heat of reaction which is the same for both does not depend on particle size. Likewise for the NS24 and SF24 systems.

Table 4: Parameters of least-squares model fit to Equation 1

Mix ID	Fit parameters, Equation 1				
	k	H_0	H_0	H_0	b
	h^{-1}	J per g paste	kJ/g SiO_2	kJ/mol SiO_2	J per g paste
NS81	0.0074	263	1.58	94.7	29.4
NS24	0.0070	169	2.03	122.2	23.7
SF81	0.0014	(265)	1.59	95.5	8.5
SF24	0.0013	173	2.08	125.0	7.4

On the other hand, the NS81 mix contains exactly twice as much silica per unit weight of paste as the NS24 mix (seeTable 4), but H_0 (per g of paste) of NS81 is significantly less than twice that of the NS24 mix. The observed ratio is 1.51. This suggests that there is unreacted residual silica in the NS81 systems, and that the true C/S ratio is greater than the nominal (molar) target value of 0.81. The same comparison can be made between the SF81 and SF24 mixes, with the same conclusion. Expressed per mol SiO_2, H_0 is essentially the heat of reaction, which is smaller for the NS81 and SF81 mixes than for the NS24 and SF24 mixes. Once again, this allows the possibility that the NS81 and SF81 mixes contain unreacted silica at the end of the reaction, and that the true C/S ratio of the C-S-H formed is greater than the nominal value. The heats of reaction are comparable with those reported for other C-S-H forming systems, but further thermodynamic analysis is outside the scope of this study.

3.2.1. Early-time behaviour and the rate maximum

The similarities between the hydration of the silica/portlandite system described here and that of the C_3S system are noteworthy. The same maximum in reaction rate can be seen in the calorimetric data on nano-silica/portlandite systems reported by Lin *et al.* [36], although it is not discussed. The existence of an early slow-reaction period is generally regarded as a particular feature of the hydration of calcium silicate systems. Yet it is observed here in a system where the Ca concentration in solution is buffered by the presence of excess solid portlandite, and where the C-S-H can only form by transport of Ca through solution to the silica surface. This is in sharp contrast to the case of C_3S hydration where both Ca and Si are co-located, and only water is required for reaction; furthermore, because the C/S ratio of the C-S-H product is <3, there must be a net outward diffusion of Ca into solution, rather than an inward transport as here. In the C_3S case, the accelerating-rate period following the minimum is generally described by means of a nucleation and growth [NG] mechanism, often using the Avrami or Cahn models, or variants. NG models ascribe the hydration kinetics to the interplay of nucleation rates and crystal-growth rates, and assume that simple diffusive transport is not rate-controlling. It is however recognised that at long times the reaction rate is likely to be controlled by diffusion of reactant species through the C-S-H to the unhydrated surface beneath. Thus the long tail in the C_3S heat-flow rate at extended times is not represented by NG models. We find that the early-time heat flow data for the nano-silica mixes NS81 and NS24 can be represented by a simple stretched-exponential Avrami model for the extent of reaction X at time t

$$X = 1 - \exp(-k_2 t^m) \tag{2}$$

where k_2 is a rate constant, and m is a constant. The heat flow rate R is proportional to $\mathrm{d}X/\mathrm{d}t$, so that for this model

$$R = amk_2^m (t - t_0)^{m-1} \exp\bigl[-[k_2(t - t_0)]^m\bigr] \tag{3}$$

where t_0 is a time-offset and a is a constant. We show results in Fig 5b, with fit parameters given in Table 5. In the data analysis, we have calculated the difference between the measured cumulative heat flow and the simple exponential model, and differentiated this numerically to obtain the non-exponential contribution. That we can fit the data with such a model does not have any clear mechanistic implications, but the existence of the rate minimum and maximum is unexpected, and future work may provide an explanation. The values of the constant m are rather lower than the typical Avrami values of 2–3. We note

Table 5: Parameters of model fit to Equation 2

Mix ID	Fit parameters, Equation 3		
	k_2	m	a
	h^{-1}	–	mW per g paste
NS81	0.054	1.50	26.1
NS24	0.030	1.52	32.7

Time-offset $t_0 = 12\,\mathrm{h}$

that of course the Avrami model (in its site-saturation form) reduces to our simple exponential form when $m = 1$.

3.3. Thermal analysis

TG/DSC curves of C-S-H samples hydrated for 28 days are shown in Figure 6. Thermogravimetric curves are typical of C-S-H with a total weight loss of 30–35%. The first thermal step is observed in the range 25–200 °C and corresponds to the evaporation of pore and capillary water and dehydration of C-S-H [26, 4]. The second weight loss occurs between 350–550 °C and is associated with the dehydroxylation of portlandite. The thermal step in the range 600–700 °C is attributed to the loss of CO_2 from calcium carbonate, due to the surface carbonation of samples during instrument operations [26]. As noted in [28], there is a small continuous weight loss over much of the temperature range, and this is attributed to continuing dehydration of C-S-H. TG results are summarised in Table 6. The weight loss values for portlandite and calcite were found by a simple tangent method [37]. The weight loss was obtained as difference in weight at the intersections of the tangent drawn at the point of maximum slope in the weight loss curve and straight lines fitted to the data above and below the decomposition.

At 28 days, samples made with nano-silica contain more C-S-H than samples made with silica fume. In agreement with Raman and XRD analysis, at the same initial stoichiometric C/S ratio, nano-silica promotes the formation of C-

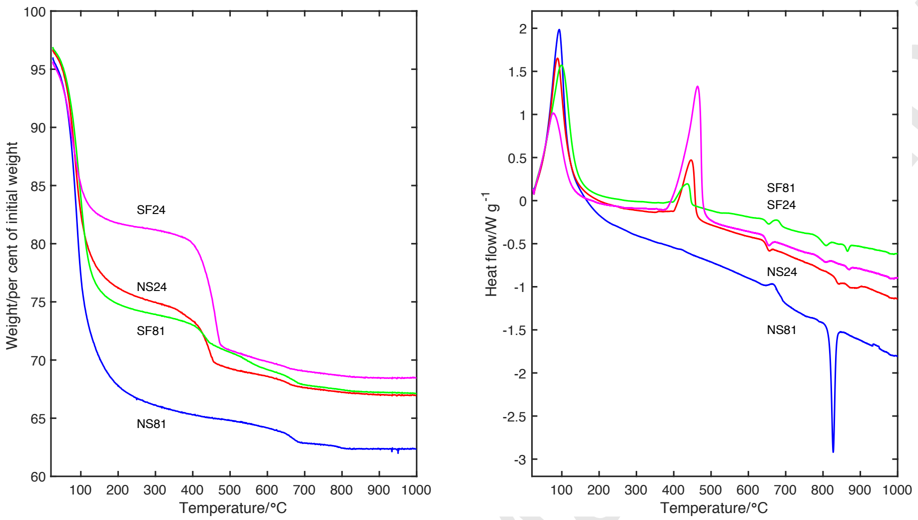

Figure 6: TG and DSC curves of all samples. Left: Thermogravimetric data; right: DSC response, exothermic reaction as downward deflection.

S-H and no $Ca(OH)_2$ is detected in the mix NS81. Additionally, the portlandite content, proportional to the weight loss, in %, in the range 350–550 °C, is higher in samples made with silica-fume, where it is up to 40 wt%. TG data were used to calculate the C/S ratio of hydrated samples (final C/S ratio at 28 days of hydration), according to the methodology described in Garbev *et al.* [38]. Results are reported in Table 7. Using nano-silica instead of silica fume as the silica source, results in an overall higher final C/S ratio. This reflects the higher reactivity of nano-silica and its capability to form additional C-S-H. The calculated C/S ratio values should be taken more as a guide rather than absolute. In sample NS081, while the reaction went to completion at 28d, the calorimetry data suggests some unreacted silica, which indicates the C/S ratio is higher than the nominal value. Sample NS24, the reaction was also complete by 28 days and the system had an excess of calcium, expressed as wt% portlandite, so it is unlikely there is any unreacted silica. The C/S value

Table 6: Composition of reacted mixes at 28 d: TG and XRD results

Mix ID	Fraction of total CaO as				
	C-S-H		Portlandite		Calcite
	TGA	XRD	TGA	XRD	TGA
NS81	0.980	1.0	0	0	0.02
NS24	0.597	0.62	0.396	0.38	0.008
SF81	0.792	0.83	0.193	0.17	0.016
SF24	0.302	0.30	0.695	0.70	0.003

Notes: Calcite was not determined by XRD analysis

of 1.7 is higher than anticipated from a synthetic C-S-H, where an upper value of 1.6 [39] is expected, this could be explained by the slow decomposition of some nano-crystalline portlandite trapped within the C-S-H pores. Calorimetry data shows that at 28 days, both silica fume samples had not finished reacting and therefore the C/S ratio is likely to be higher than calculated due to unreacted silica.

Table 7: Mix compositions at 28 d and calculated initial (nominal) and measured C/S molar ratios, from thermogravimetric analysis

Mix ID	Portlandite	Calcite	C/S	
			initial	final
	wt%		mol ratio	
NS81	0	1.3	0.81	0.79
NS24	19.3	0.65	2.4	1.70
SF81	7.3	0.88	0.81	0.66
SF24	39.5	0.22	2.4	1.02

Note: Decomposition temperature ranges: portlandite, NS24 338–495 °C, SF81 338–460 °C, SF24 338–500 °C; calcite, 630–690 °C, except NS24 625–690 °C.

The C/S ratio plays a key role in the hydration kinetics of Portland cement and its strength development [40]. In hydrated Portland cement, it varies in the range 0.6–2.0 mol/mol, and many authors have found that mortar and concrete pastes modified by the addition of pozzolanic nano-particles produce a denser C-S-H with a lower C/S ratio [41, 42, 43]. Results presented here show that at 28 days, which is the standard curing time for most applications, the C/S ratio is increased by smaller particles. This is due to the enhanced reactivity of nano-silica compared to that of silica fume. C/S ratio is a key parameter for specific application and not only in cement industry: C-S-H can be crystallographically tailored to incorporate radionuclides or heavy metals into its structure [44, 45], or could be expanded to increase porosity and be used in waste-water treatment as an adsorbent material [46, 47]. Hence, understanding the effect of fine additives on the C/S ratio and quantity is valuable.

Results of the differential scanning calorimetry of samples hydrated for 28 days (curves shown in Figure 6) are summarised in Table 8. DSC curves show the first endothermic event at about 80 °C, corresponding to the formation of C-S-H and evaporation of pore water. The integrated peak area is greater in sample NS081 (603 J g^{-1}) than sample SF081 (586 J g^{-1}). Correspondingly, the endothermic event at about 430 °C, associated with the decomposition of $Ca(OH)_2$, is greater in samples with higher nominal C/S ratio and/or larger silica particle size range (sample NS24, 195 J g^{-1}; sample SF24, 533 J g^{-1}). Furthermore, the higher C/S ratio causes a shift of the DSC peak, which represents portlandite breakdown, towards a higher temperature, and close to the peak centre of pure portlandite, at 460 °C. The DSC response of sample NS081 exhibits a narrow exothermic peak at around 800 °C, attributed to the crystallisation of wollastonite [48, 49, 44, 28].

4. Conclusions

We report the results of a study of the formation of C-S-H by reaction of amorphous silica and portlandite at low and high C/S ratio (0.81 and 2.4

Table 8: DSC peak information: peak height, centre and integrated area in the decomposition range of C-S-H (25–200 °C) and portlandite (350–550 °C)

Mix ID	C-S-H 25–200 °C			Portlandite 350–550 °C		
	centre °C	height mW/mg	area J/g	centre °C	height mW/mg	area J/g
SF81	99	1.58	586	436	0.19	66.4
SF24	78	1.02	320	464	1.32	533
NS81	93	1.99	603	–	–	–
NS24	88	1.65	496	446	0.47	195

Note: NS81, no portlandite detected

mol/mol). Two different sources of silica were used: silica fume (particle size range of 100–1000 nm) and nano-silica (particle size range of 5–20 nm). Our analysis of experimental data lead to the following conclusions.

1. The reaction yields C-S-H as the sole product, although portlandite and unreacted silica may also be present in the final composition.
2. The Raman spectra confirm the XRD and TGA evidence that there is only slight carbonation in the samples.
3. The Raman spectra reveal systematic changes with composition, notably a broadening of the Si-O-Si symmetric bending at $\sim 666\,\mathrm{cm}^{-1}$ in the NS samples with increasing C/S.
4. Isothermal calorimetry allows the rate of reaction at 25 °C to be monitored over first 200 h, and indicates a strong dependence of the reaction rate on the particle size.
5. Calorimetric data show that the overall kinetics is well described by a simple exponential model. This allows the timescale for the completion of the reaction to be estimated.
6. Heat flow rate data show the existence of a weak minimum and maximum

in the rate of reaction at 20–30 h after mixing. This feature is similar to the well known induction period in the hydration tricalcium silicate C_3S, although the latter is more pronounced. Heat flow rate data around the rate maximum can be described by a site-saturation Avrami model, with $m \sim 1.5$. The rate maximum is unexpected and deserves further study.

7. Mass balance calculations using TG and XRD composition data provide estimates of the C/S ratio of the C-S-H formed, although in the absence of any direct information on possible unreacted silica, these C/S ratios are nominal lower limits. Nonetheless, there is strong indication that the C/S of the C-S-H product increases as the C/S of the initial mix increases.

Acknowledgement

This work is supported by UK Engineering and Physical Sciences Research Council, (EPSRC Grant No. EP/L014041/1 - DISTINCTIVE Consortium - Decommissioning, Immobilisation and Storage soluTIons for NuClear wasTe InVEntories). The authors acknowledge the loan of an Raman InVia Spectrometer from the EPSRC Engineering Instrument Pool. Data associated with research published in this paper is accessible at: http://dx.doi.org/10.15129/9a6e8793-f62f-4e0e-8c97-14d4ba104f71.

References

References

[1] R. Yu, P. Spiesz, H. Brouwers, Effect of nano-silica on the hydration and microstructure development of Ultra-High Performance Concrete (UHPC) with a low binder amount, Construction and Building Materials 65 (2014) 140–150. `doi:10.1016/j.conbuildmat.2014.04.063`.

[2] Y. Qing, Z. Zenan, K. Deyu, C. Rongshen, Influence of nano-SiO2 addition on properties of hardened cement paste as compared with sil-

ica fume, Construction and Building Materials 21 (3) (2007) 539–545. `doi:10.1016/j.conbuildmat.2005.09.001`.

[3] G. Quercia, G. Hüsken, H. J. H. Brouwers, Water demand of amorphous nano silica and its impact on the workability of cement paste, Cement and Concrete Research 42 (2) (2012) 344–357. `doi:10.1016/j.cemconres.2011.10.008`.

[4] H. Biricik, N. Sarier, Comparative study of the characteristics of nano silica-, silica fume- and fly ash-incorporated cement mortars, Materials Research 17 (3) (2014) 570–582. `doi:http://dx.doi.org/10.1590/S1516-14392014005000054`.

[5] S. Dittrich, J. Neubauer, F. Goetz-Neunhoeffer, The influence of fly ash on the hydration of OPC within the first 44h- A quantitative in situ XRD and heat flow calorimetry study, Cement and Concrete Research 56 (2014) 129–138. `doi:10.1016/j.cemconres.2013.11.013`.

[6] A. Kar, I. Ray, A. Unnikrishnan, J. F. Davalos, Microanalysis and optimization-based estimation of C-S-H contents of cementitious systems containing fly ash and silica fume, Cement and Concrete Composites 34 (3) (2012) 419–429. `doi:10.1016/j.cemconcomp.2011.09.008`.

[7] R. F. Feldman, G. G. Carette, V. M. Malhotra, Studies on mechanics of development of physical and mechanical properties of high-volume fly ash-cement pastes, Cement and Concrete Composites 12 (4) (1990) 245–251. `doi:10.1016/0958-9465(90)90003-G`.

[8] A. Lazaro, G. Quercia, H. J. H. Brouwers, J. W. Geus, Synthesis of a Green Nano-Silica Material Using Beneficiated Waste Dunites and Its Application in Concrete, World Journal of Nano Science and Engineering 03 (03) (2013) 41–51. `doi:10.4236/wjnse.2013.33006`.

[9] Y. Xu, D. Chung, Cement of high specific heat and high thermal conductivity, obtained by using silane and silica fume as admixtures, Ce-

ment and Concrete Research 30 (7) (2000) 1175–1178. doi:10.1016/S0008-8846(00)00296-9.

[10] H.-W. Song, S.-W. Pack, S.-H. Nam, J.-C. Jang, V. Saraswathy, Estimation of the permeability of silica fume cement concrete, Construction and Building Materials 24 (3) (2010) 315–321. doi:10.1016/j.conbuildmat.2009.08.033.

[11] Y. Wei, W. Yao, X. Xing, M. Wu, Quantitative evaluation of hydrated cement modified by silica fume using QXRD, 27Al MAS NMR, TG-DSC and selective dissolution techniques, Construction and Building Materials 36 (2012) 925–932. doi:10.1016/j.conbuildmat.2012.06.075.

[12] G. Land, D. Stephan, The influence of nano-silica on the hydration of ordinary Portland cement, Journal of Materials Science 47 (2) (2012) 1011–1017. doi:10.1007/s10853-011-5881-1.

[13] L. Wang, D. Zheng, S. Zhang, H. Cui, D. Li, Effect of Nano-SiO2 on the Hydration and Microstructure of Portland Cement, Nanomaterials 6 (12) (2016) 241. doi:10.3390/nano6120241.

[14] M. Kumar, S. K. Singh, N. Singh, Heat evolution during the hydration of Portland cement in the presence of fly ash, calcium hydroxide and super plasticizer, Thermochimica Acta 548 (2012) 27–32. doi:10.1016/j.tca.2012.08.028.

[15] B. W. Langan, K. Weng, M. A. Ward, Effect of silica fume and fly ash on heat of hydration of Portland cement, Cement and Concrete Research 32 (7) (2002) 1045–1051. arXiv:arXiv:1011.1669v3, doi:10.1016/S0008-8846(02)00742-1.

[16] M. Oltulu, R. ahin, Pore structure analysis of hardened cement mortars containing silica fume and different nano-powders, Construction and Building Materials 53 (2014) 658–664. doi:10.1016/j.conbuildmat.2013.11.105.

[17] J. Rossen, B. Lothenbach, K. Scrivener, Composition of CSH in pastes with increasing levels of silica fume addition, Cement and Concrete Research 75 (2015) 14–22. `doi:10.1016/j.cemconres.2015.04.016`.

[18] J. J. Thomas, J. J. Biernacki, J. W. Bullard, S. Bishnoi, J. S. Dolado, G. W. Scherer, A. Luttge, Modeling and simulation of cement hydration kinetics and microstructure development, Cement and Concrete Research 41 (12) (2011) 1257–1278. `doi:10.1016/j.cemconres.2010.10.004`.

[19] Q. Zeng, K. Li, T. Fen-chong, P. Dangla, Determination of cement hydration and pozzolanic reaction extents for fly-ash cement pastes, Construction and Building Materials 27 (1) (2012) 560–569. `doi:10.1016/j.conbuildmat.2011.07.007`.

[20] H. Taylor, Cement chemistry, 2nd Edition, Vol. 20, 1998. `doi:10.1016/S0958-9465(98)00023-7`.

[21] I. Richardson, Tobermorite/jennite- and tobermorite/calcium hydroxide-based models for the structure of C-S-H: applicability to hardened pastes of tricalcium silicate, β-dicalcium silicate, Portland cement, and blends of Portland cement with blast-furnace slag, metakaol, Cement and Concrete Research 34 (9) (2004) 1733–1777. `doi:10.1016/j.cemconres.2004.05.034`.

[22] I. Richardson, L. Black, J. Skibsted, R. Kirkpatrick, Characterisation of cement hydrate phases by TEM, NMR and Raman spectroscopy, Advances in Cement Research 22 (4) (2010) 233–248. `doi:10.1680/adcr.2010.22.4.233`.

[23] X. Cong, R. Kirkpatrick, 29Si MAS NMR study of the structure of calcium silicate hydrate, Advanced Cement Based Materials 3 (3-4) (1996) 144–156. `doi:10.1016/S1065-7355(96)90046-2`.

[24] O. Mendoza, C. Giraldo, S. S. Camargo, J. I. Tobón, Structural and nanomechanical properties of Calcium Silicate Hydrate (C-S-H) formed from

alite hydration in the presence of sodium and potassium hydroxide, Cement and Concrete Research 74 (2015) 88–94. `doi:10.1016/j.cemconres.2015.04.006`.

[25] S. Nath, S. Maitra, S. Mukherjee, S. Kumar, Microstructural and morphological evolution of fly ash based geopolymers, Construction and Building Materials 111 (2016) 758–765. `doi:10.1016/j.conbuildmat.2016.02.106`.

[26] K. Garbev, M. Bornefeld, G. Beuchle, P. Stemmermann, Cell Dimensions and Composition of Nanocrystalline Calcium Silicate Hydrate Solid Solutions. Part 2: X-Ray and Thermogravimetry Study, Journal of the American Ceramic Society 91 (9) (2008) 3015–3023. `doi:10.1111/j.1551-2916.2008.02601.x`.

[27] S. Grangeon, F. Claret, C. Lerouge, F. Warmont, T. Sato, S. Anraku, C. Numako, Y. Linard, B. Lanson, On the nature of structural disorder in calcium silicate hydrates with a calcium/silicon ratio similar to tobermorite, Cement and Concrete Research 52 (2013) 31–37. `doi:10.1016/j.cemconres.2013.05.007`.

[28] E. Tajuelo, K. Garbev, D. Merz, L. Black, I. G. Richardson, Thermal stability of C-S-H phases and applicability of Richardson and Groves' and Richardson C-(A)-S-H (I) models to synthetic C-S-H, Cement and Concrete Research 93 (2017) 45–56. `doi:10.1016/j.cemconres.2016.12.005`.

[29] I. G. Richardson, Model structures for C-(A)-S-H(I), Acta Crystallographica Section B: Structural Science, Crystal Engineering and Materials 70 (6) (2014) 903–923. `doi:10.1107/S2052520614021982`.

[30] L. Black, C. Breen, J. Yarwood, K. Garbev, P. Stemmermann, B. Gasharova, Structural Features of C-S-H(I) and its Carbonation in Air: A Raman Spectroscopic Study. Part II: Carbonated Phases, Journal of the American Ceramic Society 90 (3) (2007) 908–917. `doi:10.1111/j.1551-2916.2006.01429.x`.

[31] K. Garbev, P. Stemmermann, L. Black, C. Breen, J. Yarwood, B. Gasharova, Structural features of C-S-H(I) and its carbonation in air-A Raman spectroscopic study. Part I: Fresh phases, Journal of the American Ceramic Society 90 (3) (2007) 900–907. `doi:10.1111/j.1551-2916.2006.01428.x`.

[32] P. W. Brown, J. Pommersheim, G. Frohndorff, A kinetic model for the hydration of tricalcium silicate, Cement and Concrete Research1 15 (1) (1985) 35–41.

[33] J. J. Thomas, A new approach to modeling the nucleation and growth kinetics of tricalcium silicate hydration, Journal of the American Ceramic Society 90 (10) (2007) 3282–3288. `doi:10.1111/j.1551-2916.2007.01858.x`.

[34] J. W. Bullard, G. W. Scherer, J. J. Thomas, Time dependent driving forces and the kinetics of tricalcium silicate hydration, Cement and Concrete Research 74 (2015) 26–34. `doi:10.1016/j.cemconres.2015.03.016`.
URL `http://www.sciencedirect.com/science/article/pii/S0008884615001027`

[35] S. Vyazovkin, C. Wright, Kinetics in solids, Annual Review of Physical Chemistry 48 (1) (1997) 125–149. `doi:10.1146/annurev.physchem.48.1.125`.

[36] Q. Lin, Z. Xu, X. Lan, Y. Ni, C. Lu, The reactivity of nano silica with calcium hydroxide, Journal of Biomedical Materials Research - Part B Applied Biomaterials 99 B (May) (2011) 239–246. `doi:10.1002/jbm.b.31891`.

[37] B. Lothenbach, P. Durdzinski, K. de Weerdt, Thermogravimetric analysis, in: A Practical Guide to Microstructural Analysis of Cementitious Materials, CRC Press–Taylor & Francis, 2015, Ch. 5, pp. 177–211.

[38] K. Garbev, M. Bornefeld, G. Beuchle, P. Stemmermann, Cell dimensions and composition of nanocrystalline calcium silicate hydrate solid solutions.

Part 1: Synchotron-based X-Ray Diffraction, Journal of the American Ceramic Society 91 (9) (2008) 3005–3014. `doi:10.1111/j.1551-2916.2008.02601.x`.

[39] A. Kumar, B. J. Walder, A. Kunhi Mohamed, A. Hofstetter, B. Srinivasan, A. J. Rossini, K. Scrivener, L. Emsley, P. Bowen, The Atomic-Level Structure of Cementitious Calcium Silicate Hydrate, Journal of Physical Chemistry C 121 (32) (2017) 17188–17196. `doi:10.1021/acs.jpcc.7b02439`.

[40] M. Moukwa, S. Farrington, D. Youn, Determination of Ca(OH)2 in hydrated cement paste by differential scanning calorimetry, Thermochimica Acta 195 (1992) 231–237. `doi:10.1016/0040-6031(92)80066-6`.

[41] S. Kawashima, P. Hou, D. J. Corr, S. P. Shah, Modification of cement-based materials with nanoparticles, Cement and Concrete Composites 36 (2013) 8–15. `doi:10.1016/j.cemconcomp.2012.06.012`.

[42] S. Bae, C. Meral, J.-e. Oh, J. Moon, M. Kunz, P. J. Monteiro, Characterization of morphology and hydration products of high-volume fly ash paste by monochromatic scanning x-ray micro-diffraction (μ-SXRD), Cement and Concrete Research 59 (2014) 155–164. `doi:10.1016/j.cemconres.2014.03.001`.

[43] L. P. Singh, S. K. Bhattacharyya, S. P. Shah, G. Mishra, U. Sharma, Studies on early stage hydration of tricalcium silicate incorporating silica nanoparticles : Part II, Construction and Building Materials 102 (2016) 943–949. `doi:10.1016/j.conbuildmat.2015.05.084`.

[44] A. Stumm, K. Garbev, G. Beuchle, L. Black, P. Stemmermann, R. Nüesch, Incorporation of zinc into calcium silicate hydrates, Part I: formation of C-S-H(I) with C/S=2/3 and its isochemical counterpart gyrolite, Cement and Concrete Research 35 (9) (2005) 1665–1675. `doi:10.1016/j.cemconres.2004.11.007`.

[45] E. Wieland, J. Tits, D. Kunz, R. Dähn, Strontium Uptake by Cementitious Materials, Environmental Science & Technology 42 (2) (2008) 403–409. `doi:10.1021/es071227y`.

[46] Z. Jing, F. Jin, N. Yamasaki, E. H. Ishida, Hydrothermal synthesis of a novel tobermorite-based porous material from municipal incineration bottom ash, Industrial and Engineering Chemistry Research 46 (8) (2007) 2657–2660. `doi:10.1021/ie070016z`.

[47] W. Guan, F. Ji, Z. Fang, D. Fang, Y. Cheng, P. Yan, Q. Chen, Low hydrothermal temperature synthesis of porous calcium silicate hydrate with enhanced reactivity SiO2, Ceramics International 40 (3) (2014) 4415–4420. `doi:10.1016/j.ceramint.2013.08.113`.

[48] W. Sha, G. Pereira, Differential scanning calorimetry study of ordinary Portland cement paste containing metakaolin and theoretical approach of metakaolin activity, Cement and Concrete Composites 23 (6) (2001) 455–461. `doi:10.1016/S0958-9465(00)00090-1`.

[49] D. S. Klimesch, A. Ray, J.-P. Guerbois, Differential scanning calorimetry evaluation of autoclaved cement based building materials made with construction and demolition waste, Thermochimica Acta 389 (1-2) (2002) 195–198. `doi:10.1016/S0040-6031(02)00058-8`.